Mixing-Induced Mineral Precipitation in Porous Media

Front Development and Its Impact on Flow and Transport

Kottsova, Anna; Kong, Xiang-Zhao; Zitha, Pacelli L.J.; Saar, Martin O.; Bruhn, David F.; Knornschild, Nils; Allaz, Julien M.; Archer, Corey; Brehme, Maren

DOI
10.1029/ 2024WR039316

Publication date
2025

Document Version
Final published version

Published in
Water Resources Research

Citation (APA)
Kottsova, A., Kong, XZ., Zitha, P. L. J., Saar, M. O., Bruhn, D. F., Knornschild, N., Allaz, J. M., Archer, C., & Brehme, M. (2025). Mixing-Induced Mineral Precipitation in Porous Media: Front Development and Its Impact on Flow and Transport. *Water Resources Research*, *61*(10), Article e2024WR039316. https://doi.org/10.1029/ 2024WR039316

Water Resources Research

RESEARCH ARTICLE
10.1029/2024WR039316

Mixing-Induced Mineral Precipitation in Porous Media: Front Development and Its Impact on Flow and Transport

Anna Kottsova[1,2], Xiang-Zhao Kong[1], Pacelli L. J. Zitha[2], Martin O. Saar[1], David F. Bruhn[2], Nils Knornschild[1], Julien M. Allaz[3], Corey Archer[3], and Maren Brehme[1]

[1]Geothermal Energy and Geofluids Group, Institute of Geophysics, Department of Earth and Planetary Sciences, ETH Zurich, Zurich, Switzerland, [2]Department of Geosciences and Engineering, Delft University of Technology, Delft, The Netherlands, [3]Institute of Geochemistry and Petrology, Department of Earth and Planetary Sciences, ETH Zurich, Zurich, Switzerland

Key Points:

- The precipitation front forms a curtain-like structure at the fluid interface, initially cross-flow- and later parallel-flow-controlled
- Injection flow rates strongly affect precipitation front formation; higher flow rates enhance mixing, resulting in greater accumulation
- In-situ XRCT scanning in combination with differential pressure measurements captures the real-time precipitation process and its evolution

Supporting Information:

Supporting Information may be found in the online version of this article.

Correspondence to:

A. Kottsova,
anna.kottsova@eaps.ethz.ch

Citation:

Kottsova, A., Kong, X.-Z., Zitha, P. L. J., Saar, M. O., Bruhn, D. F., Knornschild, N., et al. (2025). Mixing-induced mineral precipitation in porous media: Front development and its impact on flow and transport. *Water Resources Research*, *61*, e2024WR039316. https://doi.org/10.1029/2024WR039316

Received 29 OCT 2024
Accepted 6 JUL 2025

Correction added on 17 OCT 2025, after first online publication: The CSAL funding statement has been added.

Author Contributions:

Conceptualization: Anna Kottsova, Xiang-Zhao Kong, Pacelli L. J. Zitha, Maren Brehme
Data curation: Anna Kottsova
Funding acquisition: Maren Brehme
Investigation: Anna Kottsova, Xiang-Zhao Kong, Nils Knornschild, Julien M. Allaz, Corey Archer
Methodology: Anna Kottsova, Xiang-Zhao Kong, Pacelli L. J. Zitha, Nils Knornschild, Maren Brehme

Abstract Injectivity decline during brine reinjection poses a significant challenge in the geothermal industry, with reported cases of substantial injectivity reduction and in severe cases, complete well shutdown. Among the reasons behind these issues, chemical processes play a key role due to potential changes in the fluid properties throughout the operation cycle. When reinjected, the fluid with altered chemical composition mixes with in situ fluids, potentially triggering mineral precipitation, which can obstruct flow and reduce injectivity. To better characterize the mechanisms behind the mixing-induced mineral precipitation processes, we performed a series of core-flooding experiments combined with high-resolution imaging techniques. Our study focuses on the direct visualization of barite precipitation fronts in Berea sandstone and characterizes their spatial and temporal evolution under varying flow conditions. Pressure response and time-resolved 2D scanning were analyzed to capture real-time changes in the system, whereas post-experiment micro-CT scanning, electron microprobe analysis, and mass spectrometry were employed to examine the morphology and distribution of the mineral deposits. Our results highlight the critical role of flow velocities on the kinetics of mixing-induced precipitation and demonstrate how mineral accumulation may significantly reduce permeability. These findings provide valuable insights into the dynamics of mineral precipitation in porous media, highlighting the impact of flow conditions on formation damage in geothermal systems.

Plain Language Summary Injectivity decline, or the reduced ability to inject fluids into a geothermal well, is a significant challenge in geothermal energy production. A primary contributor to this problem is the mixing of reinjected fluids with natural underground fluids, which can trigger chemical reactions and lead to mineral buildup. This buildup, known as mineral precipitation, can block fluid pathways, making it harder to continue fluid injection and reducing the system's efficiency. To understand this process better, we conducted laboratory experiments on rock samples using advanced imaging techniques to observe how the reaction unfolds. Our study focused on barite mineral formation when two reacting fluids mix under different flow conditions. We found that the injection rate directly impacts how quickly the reaction occurs, how far it spreads in the rock, and how much it affects the rock's properties. These findings offer valuable insights into how flow conditions influence permeability in geothermal systems.

1. Introduction

Geothermal energy, a promising sustainable energy source, critically depends on the effective management of a subsurface system. One key aspect of this is the reinjection of produced geothermal brine, required for recharging a reservoir or complying with environmental regulations (Axelsson, 2012; Kaya et al., 2011; Luo et al., 2023). Despite its numerous benefits, reinjection often leads to significant performance reduction, with multiple geothermal projects reporting injectivity decline between 60% and 90% and, in extreme cases, complete shutdown of wells (Brehme et al., 2019; Kottsova et al., 2022; Luo et al., 2023). To address these challenges, various mitigation methods such as well stimulation, the use of scale or corrosion inhibitors, and adjustment of the injection temperature have been proposed. However, the effectiveness of these methods varies, with some wells never regaining the initial injectivity (Brehme et al., 2019). This underscores the need for a thorough understanding of the underlying mechanisms of injectivity decline.

The reasons behind these issues often lie in an interplay between physical, chemical, and biological processes. Among them, chemical processes, while not always dominant, play a critical role due to their potential for mineral

Resources: Nils Knornschild
Supervision: Pacelli L. J. Zitha, Martin O. Saar, David F. Bruhn, Maren Brehme
Visualization: Anna Kottsova
Writing – original draft: Anna Kottsova, Julien M. Allaz, Corey Archer
Writing – review & editing: Xiang-Zhao Kong, Martin O. Saar, David F. Bruhn, Maren Brehme

precipitation, both in the surface facilities and within the subsurface formations. Throughout fluid production and heat extraction, various phenomena, such as scaling, corrosion, bacterial activity, etc., may alter the original chemical composition of formation fluids (Luo et al., 2023). Practices such as co-injection of another fluid to compensate for the pressure losses in vapor-dominated systems (Majer & Peterson, 2007; Stark et al., 2005) can introduce an additional change of chemical composition. Notably, cases of co-injection of sulfate-rich seawater into geothermal fields, leading to complications, have been reported (Rosenbauer et al., 1992).

As the altered fluid is reinjected, differences in composition between injected and in situ fluids, along with temperature and pressure changes, can trigger mineral precipitation in the near-wellbore zone (Szanyi et al., 2014; Yildirim & Simsek, 2003), leading to injectivity decline. It is therefore imperative to understand in detail the processes of fluid mixing and the induced precipitation in porous media to develop more effective prevention and mitigation strategies.

Numerous experimental and numerical studies have investigated the precipitation processes in porous media and their effect on rock properties and fluid transport (Bray et al., 2016; Orywall et al., 2017; Shafabakhsh et al., 2024). For example, Bray et al. (2016) recreated calcite precipitation in artificial porous media by co-injecting Na_2CO_3 and $CaCl_2$ solutions. While they managed to visualize the front propagation by means of magnetic resonance imaging, their method did not allow high-resolution imaging of the pore space. A more recent study by Shafabakhsh et al. (2024) utilized 4D Neutron Imaging to capture the flow velocity field alterations due to calcite precipitation. However, their focus was not on detailed visualization of the precipitation front growth and propagation but rather on the resultant velocity field changes. They supplemented their studies with micro-CT scanning, which provided insights into the general front distribution post-experiment, yet without continuous real-time monitoring throughout the precipitation process.

Similarly, Poonoosamy et al. (2020) conducted MRI-assisted core-flooding experiments to study interactions between rock substrates and reactive fluids. While this approach provided insights into how barite precipitation can alter porosity and permeability, it primarily addressed rock-fluid interactions. The method itself allowed for in situ observation of macroscopic changes, supplemented with post-mortem scanning electron microscopy (SEM) to determine porosity reduction at high resolution.

Orywall et al. (2017) recreated reservoir conditions to study the process of barite precipitation under elevated pressure and temperature, highlighting the strong effect of chemical clogging on rock permeability. In their study, two incompatible fluids were mixed at the core inlet and the resulting solution was injected into the core, to initiate the precipitation process in situ. This methodology assumes well-mixed reactants, however, does not account for the effect of heterogeneous mixing directly in the pore space, which could significantly affect the precipitation behavior. Similar to other studies, visualization of barite deposits and their distribution was only performed after the experiment termination using SEM.

Injection scheme strongly governs fluid mixing and mass transport in porous media. The impact of this parameter on mineral precipitation has been examined in various studies. For instance, Yang et al. (2024) combined reactive transport modeling with microfluidic experiments to identify patterns of mixing-induced precipitation at different flow regimes. In this context, research papers on salt precipitation during CO_2 injection offer additional insights into the evolution of mineral precipitation and its effects on rock properties (Ahkami et al., 2020; Lima et al., 2021). Specifically, Ahkami et al. (2020) conducted lattice Boltzmann simulations to demonstrate how precipitation in the dual-permeability fractured porous medium is governed by the kinetics and transport processes, characterized by Damköhler and Péclet numbers. Their work revealed distinct propagation patterns that govern mineral deposition and consequent permeability changes. While these findings are significant, they underscore the need for further experimental validation, particularly to better understand fluid mixing and the onset of precipitation directly in the porous domain.

The studies conducted so far have not been able to provide continuous imaging throughout the precipitation process, nor fully account for the direct interaction of fluids in the pore space. These aspects are considered in our study, where we advance the current understanding of mineral precipitation dynamics by focusing on the direct visualization of chemical clogging in the pore space caused by the co-injection and mixing of incompatible fluids. By using core-flooding experiments, alongside high-resolution micro-CT scanning before and after the experiments, and continuous 2D scanning, we aim to provide detailed insights into the dynamics of mineral precipitation, front propagation, and evolution. This comprehensive approach enables deeper in situ monitoring of the

processes, complemented by post-experimental electron microprobe and mass spectrometry analyses for detailed characterization of formation damage, mineral precipitation, and reaction kinetics.

2. Materials and Methods

2.1. Porous Media

We selected Berea sandstone for our core-flooding experiments as it can be considered inert (with respect to the precipitation reaction of interest) and homogeneous, thereby allowing us to focus on fluid-fluid interactions. The rock was obtained in blocks from Kocurek Industries (Texas, USA), and cylindrical cores were further drilled to a diameter of 2.50 ± 0.02 cm and precisely machined to a length of 15 ± 0.1 cm. Its porosity is measured to be 20 ± 0.04%, and its permeability ranges from 50 to 80 mD. The pore volume (PV) of each core sample is thus estimated to be roughly 15 cm^3. X-ray diffraction analysis indicates that our Berea sandstone predominantly consists of quartz (ca. 92%) with kaolinite and dolomite inclusions (Figure S1 in Supporting Information S1). Therefore, usage of this rock ensures repeatability among experiments and minimizes the involvement of incidental rock-fluid interactions.

2.2. Fluids

To study mineral precipitation during the mixing of incompatible fluids, we chose the reaction of barite formation. We selected barite as the precipitating mineral due to its two key characteristics. Firstly, the density of barite, at 4.48 g cm^{-3}, is significantly higher than that of Berea sandstone, which has a density of 2.65 ± 0.01 g cm^{-3}. The substantial difference in density provides sufficient contrast in the attenuation coefficients, obtained by X-ray CT scanning, to distinguish the deposited barite from the rock matrix. Secondly, barite's low solubility in water (2.43 mg L^{-1} (Haynes, 2014)) and fast reaction kinetics (Zhen-Wu et al., 2016) ensure its precipitation at the fluid contact, making it an ideal candidate for studying the effect of mineral precipitation on flow and transport.

During the experiments, two fluids were injected into the core: sodium sulfate (Na_2SO_4) and barium chloride ($BaCl_2$) solutions, both with a starting concentration of 10 mM to ensure mineral precipitation during fluid mixing yet avoid immediate clogging at their injection points. Furthermore, potassium chloride KCl was added to the $BaCl_2$ solution at a concentration of 60 mM to serve as an inert tracer for further chemical analysis of the effluent. Upon fluid mixing, barite is expected to form according to the following reaction:

$$BaCl_2 + Na_2SO_4 \rightarrow BaSO_4\downarrow + 2NaCl. \quad (1)$$

2.3. Experiment Setup and Procedure

The goal of this study was to replicate mineral precipitation due to fluid mixing directly in the pore space. We achieved this goal by conducting core-flooding experiments with a special injection scheme, as illustrated in the schematic of the setup in Figure 1.

Prior to the experiment, the rock cores were dried in an oven for 24 hr and further radially sleeved with a thin layer of epoxy resin to prevent side-wall flow, ensuring that fluid flow occurs only within the cores. Penetration of resin was estimated on thin sections after the experiments and was shown to reduce the effective core diameter by approximately 2 mm. The samples were encased in a second layer of epoxy resin directly in the core holder and cured for 48 hr. The holder was then equipped with two injection points: a main axial injection from the top face downwards, which defines the background flow, and a side injection point of 1.2 mm in diameter 2 cm below the core top. Both top and bottom faces of the rock core were covered with endcaps, designed with a fluid distribution network to achieve even fluid seepage through the top and bottom cross sections.

The core holder was placed vertically inside the X-ray micro-CT scanner to monitor the precipitation front propagation continuously. Using a standard metal core holder was not feasible for multiple reasons. Firstly, metal has high X-ray attenuation, absorbing a significant portion of the X-ray beam, which leads to decreased quality of the image and reduction of the contrast between the rock features. Secondly, the presence of metal can introduce imaging artifacts, thus reducing the accuracy of the analysis (Kastner & Heinzl, 2020). Therefore, we designed and 3D-printed an X-ray-transparent polymer core holder using Tough2000 Resin from Formlabs. Such an approach allowed a flexible selection of the rock parameters, that is, length and diameter, as well as placement of the injection point and pressure measurement points.

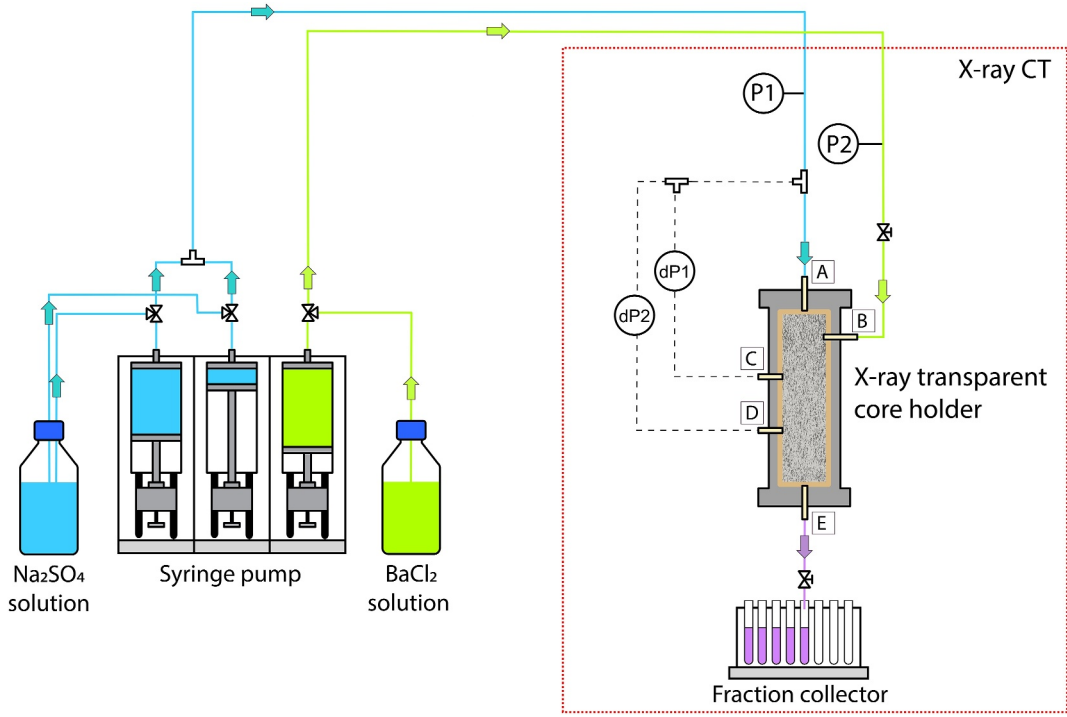

Figure 1. Schematic drawing of the core-flooding system, where two incompatible fluids (Na_2SO_4 and $BaCl_2$) are injected simultaneously into a core holder positioned inside the X-ray micro-CT scanner (injection points A and B, respectively). The effluent is continuously sampled at the outlet (E) using a fraction collector. Pressure sensors P1 and P2 measure absolute pressure, and differential pressure sensors dP1 and dP2 register pressure drop across the top (C) and middle (D) sections of the core, respectively.

Through the injection lines, the core holder was connected to CETONI Nemesys syringe pumps, set to constant flow rate injection. Pressure in the injection lines was recorded by the pressure transmitters with an accuracy of ±5 mbar. We also introduced two differential pressure sensors with an accuracy up to ±1.5 mbar, at 5 and 10 cm distance from the top face of the core respectively. This allowed us to monitor the pressure changes in three distinct sections–namely top, middle, and outlet sections–of the core sample, to further assess permeability variations along the fluid flow path. Here, the top section refers to the region from the top inlet to the dP1 measuring point (A–C Section in Figure 1), the middle section spans from the dP1 measuring point to the dP2 measuring point (C−D Section), and the outlet section extends from the dP2 measuring point to the outlet (D−E Section). The outlet was connected to a fraction collector, where we sampled effluent in fractions between 1/15 and 1/2 pore volume (PV) at atmospheric pressure. The effluent was later analyzed using inductively coupled plasma mass spectrometry (ICP-MS) to determine concentrations of cations, providing additional information about the chemical reaction progress and solute transport.

The core was first saturated and equilibrated with the background Na_2SO_4 solution, and the bulk permeability, k [L^2], was determined according to Darcy's law:

$$k = \frac{Q\mu L}{A\Delta P} = \frac{q\mu L}{\Delta P}, \tag{2}$$

where Q [$L^3\ T^{-1}$] is the volumetric injection rate uniformly distributed on a cross-sectional area, A [L^2], μ [$M\ L^{-1}\ T^{-1}$] is the dynamic viscosity, q [$L\ T^{-1}$] is the specific discharge, and ΔP [$M\ L^{-1}\ T^{-2}$] is the pressure drop across the relevant distance, L [L].

To quantify the effect of formation damage, following the method by Bedrikovetsky et al. (2001), we determine the impedance index, J [–], as

$$J = \frac{k_0 \Delta P}{q\mu L} = \frac{k_0}{k}, \tag{3}$$

where k_0 is the initial bulk permeability (i.e., before the precipitation reaction). The impedance growth coefficient, m [–], and the formation damage coefficient, β [–], are linked to the impedance index as follows:

$$J = 1 + \frac{qt}{\phi L} m = 1 + \frac{qt}{\phi L} \frac{M_{BaSO_4} C^0_{Ba^{2+}}}{\rho_{BaSO_4}} \beta, \tag{4}$$

where ϕ [–] is the porosity, t [T] is the time, M_{BaSO_4} [M N^{-1}] is molecular weight of barite, ρ_{BaSO_4} [M L^{-3}] is barite's density, and $C^0_{Ba^{2+}}$ [N L^{-3}] is the initial concentration of the reactants. For the derivation of Equation 4 and its corresponding assumption, please refer to Text S2 in Supporting Information S1 and Bedrikovetsky et al. (2001).

Once the background flow of the axial injection reached the steady state, side injection of the $BaCl_2$ solution was started, inducing the mixing of reactive fluids and barite precipitation. The fluids were injected until the pressure reached the sensor measurement limit. After experiment termination, the permeability change was again measured by injecting the Na_2SO_4 solution at various injection rates.

2.4. Experimental Parameters

We performed three core-flooding experiments with injection flow rate being the primary variable, to determine its effect on the deposition and distribution of the precipitated barite. At reservoir conditions, background groundwater flow has low fluid velocity, while the flow of the reinjected geothermal fluid typically comes at a high interstitial velocity, depending on the distance from the injection point. We selected the flow rates for the experiment by scaling down the flow conditions in a field-case scenario to the laboratory scale, following the work of Raies et al. (2023). In a general form, the interstitial velocity can be defined as follows:

$$v = \frac{Q}{A\phi}. \tag{5}$$

For a radial flow from a fully penetrating well into a homogeneous reservoir with a thickness of h [L], the cross-sectional area A [L^2] at a distance of r [L] from the wellbore center can be calculated using the following equation:

$$A = 2\pi r h, \tag{6}$$

The resulting pore velocity profile is illustrated in Figure S2 in Supporting Information S1.

For the laboratory scale, A is calculated separately for the main and side injection and corresponds to the cross-sectional area of the injection point:

$$A_{main} = \frac{\pi d_c^2}{4}, \tag{7}$$

$$A_{side} = \left(\frac{\pi d_b^2}{4} + \pi d_b l \right), \tag{8}$$

where d_c [L] is the core sample diameter, and d_b [L] and l [L] are the diameter and the length of the injection "borehole," respectively.

In the laboratory setting, differences in velocity between the background and injection flows were established by using injection points with different cross-sectional areas. Since the pore velocity is inversely proportional to the injection area, following Equation 5, this method created the desired difference between the injection and the background velocity. For the top (background) flow, represented by Na_2SO_4 solution, the area is equal to the

Table 1
Experimental Scenarios and Corresponding Injection Parameters

Parameter	Experiment 1	Experiment 2	Experiment 3
Scenario	Low flow rate	High flow rate	Mixed flow rate
Main Injection Rate, Q_{main} (cm^3 min^{-1})	0.60	1.02	0.60/1.02
Side Injection Rate, Q_{side} (cm^3 min^{-1})	0.09	0.18	0.09/0.18
Injection Rate Ratio	6.7:1	5.7:1	6.7:1/5.7:1
Main Interstitial Velocity (cm min^{-1})	0.70	1.19	0.70/1.19
Side Interstitial Velocity (cm min^{-1})	1.98	3.95	1.98/3.95
Interstitial Velocity Ratio	1:2.8	1:3.3	1:2.8/1:3.3

cross-sectional area of the core (4.3 cm^2), while the area for the side $BaCl_2$ injection is only 0.23 cm^2. Based on this, in combination with the limitations of the pump capabilities to ensure pulsation-free injection, we selected two sets of velocities, representing low and high flow rate scenarios, shown in Table 1 and Figure S1 in Supporting Information S1.

In this study, we present the results of three core-flooding experiments: Experiment 1 under low flow rate conditions, Experiment 2 under high flow rate conditions, and Experiment 3 where the injection rates were increased after 2 pore volumes (PVs), combining the conditions of the first two experiments. The detailed experimental parameters are shown in Table 1. Beyond examining the effect of flow rate, we also investigated the impact of the injection scheme. In Experiment 1, the side $BaCl_2$ injection began only after the background flow had reached steady state, whereas in Experiments 2 and 3, the side injection flow was initiated simultaneously with the background flow.

2.5. X-Ray Computed Tomography (XRCT)

We performed 3D micro-CT scanning of the samples before and after the experiment to evaluate the overall accumulation and localization of barite precipitation in the core sample. Scanning was performed at 130 kVp and 123 μA, reaching a spatial resolution of 12.2 µm. After volume registration of the pre- and post-experiment images, we subtracted the pre-experiment image from the post-experiment one to effectively isolate and visualize the precipitated barite. To account for potential shifts in depth or angle during volume registration, we evaluated the maximum correlation between the 2D cross sections using the Pearson correlation coefficient. This approach helped identify the best-matched images for effective comparison. Data processing was performed using the Pydicom (Mason et al., 2023) and Scipy (Virtanen et al., 2020) libraries in Python, along with PerGeos® 2021 software.

Given the desired spatial resolution over a large scanning volume and the relatively fast rate of barite precipitation, time-resolved 3D scanning throughout the experiments was not feasible. Alternatively, we acquired 2D radiographs in situ at a 17-min interval, providing a time-lapse view of the precipitation process. The CT radiograph is a 2D image that represents the attenuation of the X-ray beam through the object. As a result, the radiograph reflects a compressed view of a 3D object, illustrating the internal features. By subtracting the baseline radiograph taken before the experiment, we were able to visualize the accumulation of the precipitated barite in the rock sample.

2.6. Inductively Coupled Plasma Mass Spectrometry

To monitor the progress of the chemical reaction and solute transport, we utilized ICP-MS. With it, we analyzed the cationic composition of the effluents to establish a breakthrough curve and gain insights into the solute transport of the reactants. An aliquot of each effluent was taken for concentration analysis on a Thermo-Fisher Element XR sector-field inductively coupled-plasma mass spectrometer at ETH Zurich (Vance et al., 2016). Measured intensities were converted to concentrations using a single-point calibration relative to an in-house multi-element primary standard, using bracketing by this standard to correct for any instrumental drift.

Knowing that both SO_4^{2-} and Ba^{2+} are consumed in a reaction, comparing the breakthrough curves of the nonreactive Na^+ and tracer K^+ with those reactive ones Ba^{2+} and SO_4^{2-} yields a better understanding of the interplay between reaction kinetics and transport of reactants. Accuracy and precision were assessed using two secondary multi-element standards: National Research Council of Canada river standard SLRS6, and USGS shale standard SGR1. The concentrations obtained matched certified values to within 5%–10% for both Na and K. Precision (2sd) of analysis was assessed by multiple analyses of both standards ($n \geq 10$) during the course of the experiment and was better than 5% for both elements.

As it was not possible to directly measure negatively charged SO_4^{2-} ions with the available analytical setup, we estimated its concentration indirectly by measuring the sulfur (^{32}S) content, also using ICP-MS, and by normalizing it to a single element S standard. Precision and accuracy of these analyses were also determined by repeat analyses of USGS standard SGR-1. The S concentrations obtained for these analyses also matched the certified value within 10% and with a precision (2sd) of 5%. Na and S were determined using the Element's medium resolution mode and K was determined using high-resolution mode.

It was expected that barite particles would be formed in the effluents after the breakthrough of both Ba^{2+} and SO_4^{2-}. To dissolve any potentially formed particles and ensure the quality of the mass spectrometry analysis, we added 1 ml of 50 mM solution of disodium ethylene diamine tetraacetic acid (EDTA) to each tube along with NH_4OH, as the solubility of barite in EDTA notably increases with pH (Al-Kaabi et al., 2023). The samples were further diluted 2,500 times with HNO_3 to achieve concentration levels, suitable for the ICP-MS analysis.

In this work, we only present the results of the ICP-MS measurements for Experiment 1. The effluent was collected in different increments in volume: we first used small fractions of 1 ml during the injection of the first 1/4 pore volume (PV), followed by fractions of 3.5 ml until the injection of 1 PV and afterward fractions of 7 ml. However, this approach introduced higher uncertainty in the measured concentrations for the small sample volumes.

2.7. Electron Probe Micro-Analysis

To complement the 12.2-μm spatial resolution of the micro-CT scanner, we utilized an electron probe micro-analyzer (EPMA) to examine the micro-structure of the precipitated barite within the pore space and evaluate its impact on local porosity. For this analysis, the core from Experiment 2 was cut into several thin sections perpendicular to the main flow. To avoid major impact on the rock structure and preserve the deposited material in the pore space to the maximum extent, thin sections were precisely cut using a diamond wire saw and impregnated with epoxy resin. The samples were afterward polished to a 1-μm finish and coated with a 20 nm carbon layer to ensure conductivity during analysis.

The samples were analyzed on a JEOL JXA-8230 Electron Probe Microanalyzer at ETH Zurich. First, we collected a qualitative element mapping of Barium (Ba Lα), Sulfur (S Kα), Calcium (Ca Kα), Magnesium (Mg Kα), and Aluminum (Al Kα) using wavelength dispersive spectrometers and Si, Fe, Na and K by energy dispersive spectrometry (EDS) at 15 keV acceleration voltage, 50 nA beam current, at 5 μm and 50 ms dwell time per pixel to reveal the location of all $BaSO_4$ precipitates. Here, Kα and Lα are the X-ray emission lines. It turned out that the barite particles were too small and hardly visible on such element maps and this approach was time-consuming. We therefore further identified the barite precipitates by collecting backscattered electron (BSE) images and EDS spectra at 15 keV, 20 nA, focused beam (ca. 0.7 μm) and a few seconds of collection time on a 30 mm^2 JEOL SDD EDS detector.

3. Results

In this section, we present the results of the three core-flooding experiments, highlighting the effects of varying flow rates while maintaining consistent concentrations of the injection fluids. First, we evaluate the evolution of pressure and permeability against the injected solution volume, and determine the formation damage coefficients. Next, we assess the progression and spatial distribution of precipitation using XRCT and SEM-BSE images. All evolution is displayed with respect to the injected pore volumes (PVs) of $BaCl_2$ solution, as it drives the precipitation progression. Additionally, we provide breakthrough curves for target elements in the effluent. The injection process was terminated when the pressure reached the standing limit of the injection valves (ca. 8 bar), leading to a different number of pore volumes injected in each experiment.

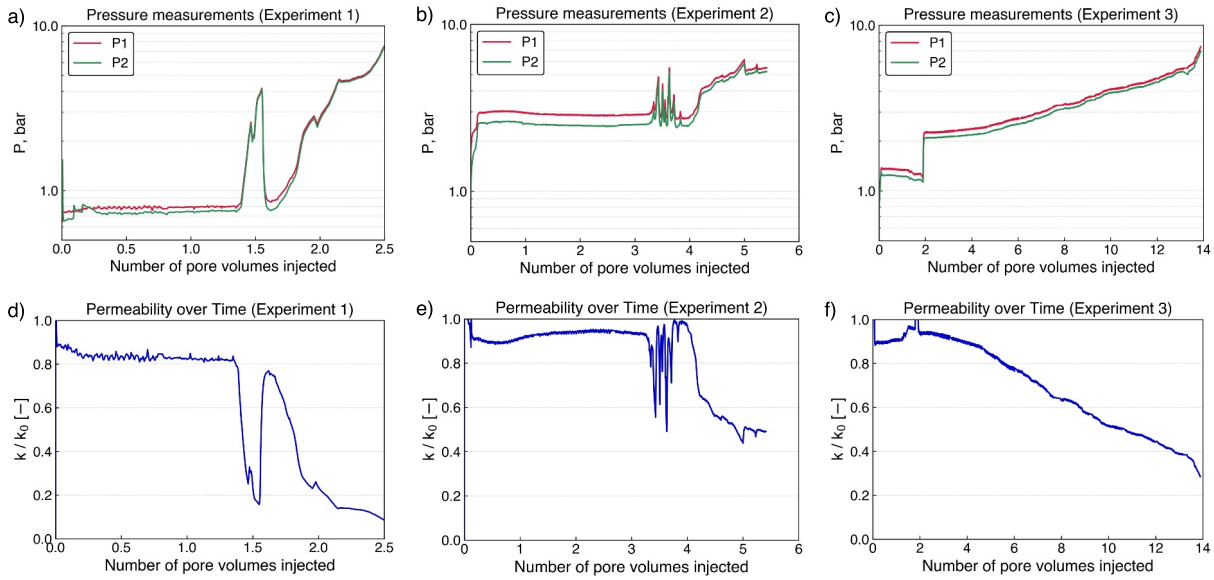

Figure 2. Evolution of pressure and normalized bulk permeability for the three experiments. Panels (a–c) demonstrate pressure changes over time, where P1 represents the inlet pressure of the main axial flow (top injection) and P2 corresponds to the inlet pressure of the side injection. Panels (d–f) show normalized permeability, k/k_0 (i.e., the reciprocal of the impedance index) for each respective core sample. The sharp fluctuations observed in Experiments 1 and 2 are attributed to temporary blockages in the outlet tubing.

3.1. Pressure Response and Permeability Evolution

Pressure measurements from the two injection points, namely, the top and the side injections, for all three experiments are depicted in Figure 2. By taking the inlet pressure (P1) of the main axial flow and the sum flow rate of the top and side injections, we calculated the bulk permeability (k) following Darcy's law (Equation 2). Taking the summation injection rate accounts for the contribution of the side flow to the overall pressure increase. By doing so, we effectively highlight the impact of solely barite precipitation on permeability. To account for the variability in bulk permeability across experiments, we present the reciprocal of the impedance index, $1/J = k/k_0$ in every experiment for consistent comparison. In the following discussion, we refer to it as the normalized permeability.

Despite variations in pressure due to different flow rates used in the experiments, the overall trends in pressure exhibit consistent behavior: a moderate initial increase in pressure followed by a stabilization period during the first several pore volumes injected. In the second half of every experiment, we observed a steady increase in pressure, attributed to the deposition of precipitated barite in the outlet endcap (outside the rock sample). Additionally, Experiments 1 and 2 show high-amplitude pressure oscillations in the middle of the experiment. These oscillations are attributed to the iterative cycle of clogging and subsequent clearance in the outlet endcap and tubing.

The change in the normalized bulk permeability over time is also consistent across the three experiments (Figures 2d–2f). Firstly, we observed a sharp drop in permeability, up to ca. 10% immediately after the introduction of the side flow, followed by an additional 5%–10% decrease during the injection of the first 1/4 PV. The normalized bulk permeability further remained stable until beginning to decrease drastically, reaching overall between 20% and 40% of the initial values. The switch from a low to a high flow rate after 2 PVs led to a slight improvement in bulk permeability.

While the two inlet pressure signals remain stable for an extended period, differential pressure measurements provide critical insights into the progression of the precipitation front within the core sample. Figure 3 demonstrates the evolution of normalized sectional permeability in the top and middle sections of the core over time. Here, the normalization is performed relative to the initial permeability of individual sections. The general trends of sectional permeability follow those observed in the bulk permeability but offer additional detail not captured by the two inlet pressure sensors. In addition to normalized permeability, Figure 3 presents impedance index, J, and

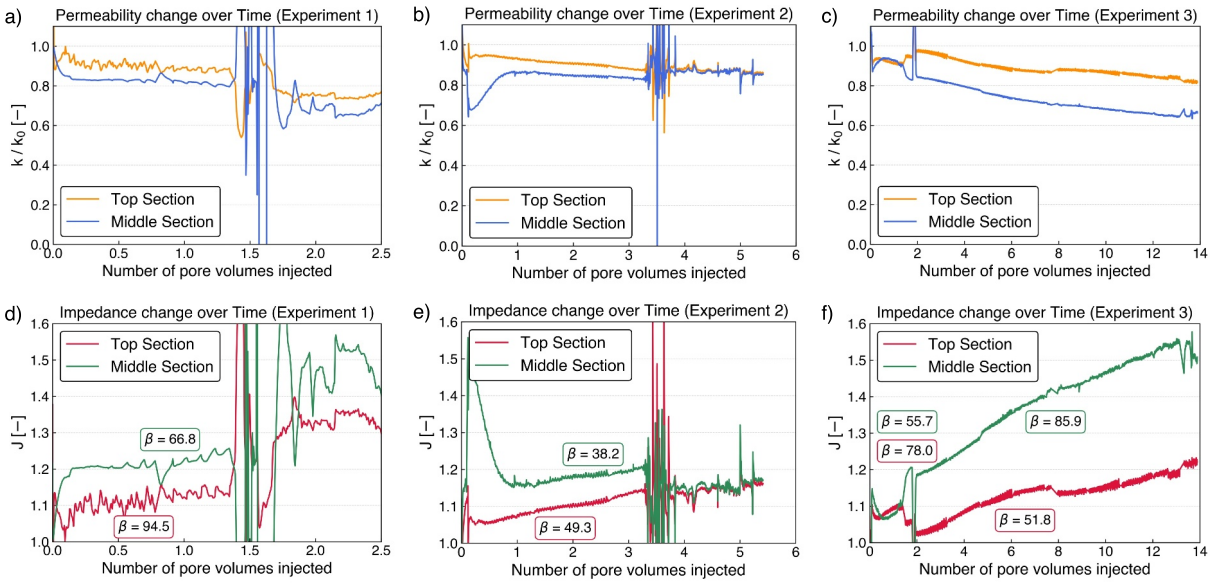

Figure 3. Temporal evolution of normalized permeability, k/k_0 (Panels a–c) and impedance index, J (Panels d–f), for the top and middle sections of the core sample, calculated from the differential pressures recorded by the sensors dP1 and dP2, respectively.

formation damage coefficient, β, for the top and middle sections. We present only the data for the top and middle sections in order to focus on mineral precipitation within the core, excluding external effects, that is, outlet endcap blockage.

The start of side injection induces an immediate drop of ca. 10% in the normalized sectional permeability, similar to the bulk permeability behavior. However, key differences are observed: the top section exhibits a partial recovery in permeability, followed by a continuous decline, while the middle section shows no recovery in Experiment 1 and partial recovery for Experiments 2 and 3. This partial recovery in the middle section in Experiments 2 and 3 is attributed to the injection scheme, where side injection flow was started simultaneously with the background flow, resulting in a more gradual establishment of the steady-state conditions. In addition, the effects of pressure oscillations are reflected in the sectional permeability. Unlike bulk permeability, which primarily displays downward oscillations, sectional permeability fluctuates around the overall trend. This behavior is explained by the design of the differential pressure transducer, which measures the pressure difference between the inlet and the core. When a blockage occurred at the outlet, the side of the sensor connected to the core registered the pressure changes more quickly than the side connected to the inlet, initially producing negative values. As the blockage cleared, the pressure stabilized, leading to the observed oscillations.

All experiments consistently show lower permeability in the middle section compared to the top section. This consistency is expected, as barite precipitation in the top section began only from the side injection point, located 2 cm from the top of the core, while in the middle section, precipitation extended across its entire length. This observation was further confirmed with XRCT imaging, discussed in the following section. Notably, during the second half of Experiment 2, a slight improvement in the middle section permeability was observed after the period of pressure oscillations. This improvement is likely attributed to the removal or redistribution of barite deposits caused by the flow oscillations in the middle section.

The formation damage coefficient offers a complementary quantitative perspective on precipitation progression. Due to the specific injection scheme in our experimental design, involving co-injection of orthogonally placed streams, the initial stage of each experiment represents a transient flow regime and initial precipitation boundary establishment. Therefore, we calculate the formation damage coefficient only within the established flow regime, identified by the onset of linear impedance growth.

In contrast to the permeability measurements, formation damage coefficient in the top section is consistently higher than in the middle section by a factor of 1.3–1.4, the only exception being the latter stage of Experiment 3. There, following a flow rate change, the coefficient for the middle section overcomes that of the top. A

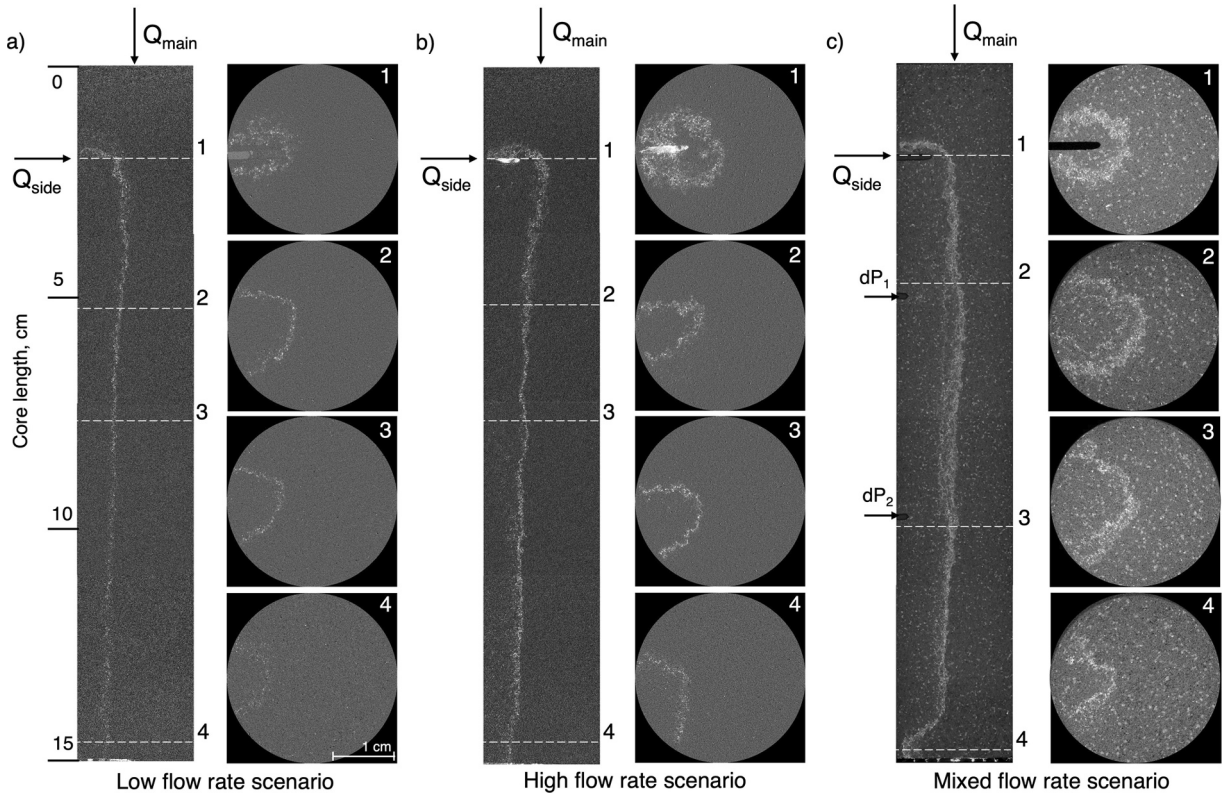

Figure 4. Coronal (vertical) and axial (horizontal) cross sections of XRCT images showing the barite precipitation profiles for (a) Experiment 1, (b) Experiment 2, and (c) Experiment 3. The dashed lines (1–4) indicate the locations of the axial cross sections along the core. Precipitated barite is visible as bright spots in the images. The images in (a, b) were generated by subtracting the registered pre- and post-experiment scans, while the images in (c) show the raw post-experiment scan, which contains natural rock inclusions.

comparison between low- and high-flow rate scenarios shows a notable reduction in the formation damage coefficient, from 94.5 to 66.8 in Experiment 1 to 49.3 and 38.2 in Experiment 2 for the top and middle sections, respectively.

3.2. Precipitation Pattern and Its Micro-Structure

Figure 4 presents coronal (vertical) cross sections alongside multiple axial (horizontal) cross sections, obtained with post-experiment micro-CT scanning. The positions of the axial cross sections are marked by the dashed lines in the vertical cross sections. These images reveal a consistent pattern of precipitation behavior across all three experiments. The precipitation boundary delineates the mixing front between the two incompatible fluids, forming a distinct "curtain" shape that follows the flow of the side injection solution. The narrow thickness of this curtain suggests limited propagation of fluids and restricted mixing within the rock matrix. A "shelter hut" structure is observed above the injection point, showing that the $BaCl_2$ solution initially propagates slightly against the main flow before being diverted downstream. Despite minor variations due to rock heterogeneity, the curtain shape extends uniformly along the core, gradually diminishing toward the outlet.

A notable observation across all experiments is the significant accumulation of precipitated barite in the outlet endcap, as seen from the bright spots at the bottom of vertical cross sections. This accumulation was further confirmed upon the disassembly of the core holder.

Despite the similarity in the shape of the precipitation front, there are notable differences between the low and high flow rate experiments, particularly in the thickness of the front. In Experiment 1, with the lower injection rate, the front has an average thickness of 0.4 mm, reaching a maximum of approximately 1 mm. In contrast, Experiment 2, with the higher injection rate, produces a thicker front, with an average of about 0.8 mm and a maximum of 1.8 mm.

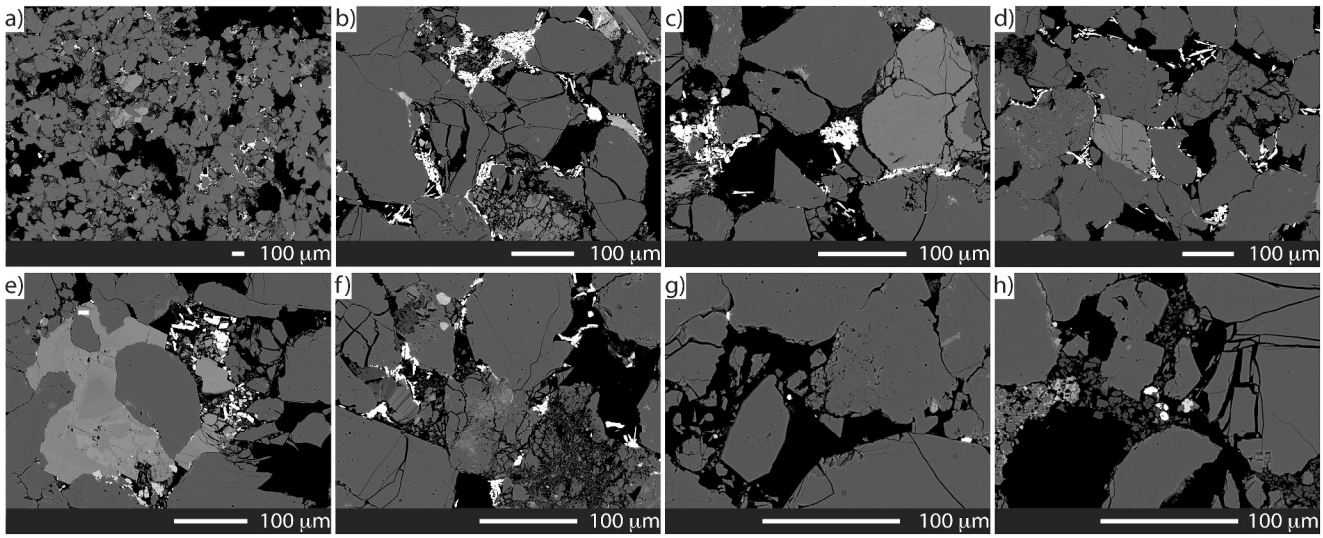

Figure 5. Backscattered Electron (BSE) images of a thin section from Experiment 2, captured at magnifications between 40× and 500×. Panels (a–f) show images from the precipitation boundary, while (g, h) depict areas inside the precipitation curtain (i.e., the region flooded by the $BaCl_2$ solution). The specific locations of these images correspond to the XRCT axial cross section shown in Figure S3 in Supporting Information S1. Here, barite is represented by the bright white regions.

Additionally, variations in injection rates lead to distinct shapes of the precipitation front around the injection borehole, highlighted in axial cross sections at Position 1 in Figures 4a and 4b. Higher side injection rate during Experiment 2 enhances the lateral component of the flow, intensifying front propagation around the injection borehole. In Experiment 2, we also observe the blockage of the side injection borehole due to the deposition of precipitated barite. It is inferred that the blockage occurred due to an early opening of the side injection valve, leading to the early mixing of reactive fluids in the injection borehole. While this affected the circular shape of the front around the injection point, it did not influence other experimental observations.

Figure 4c shows a distinct layering pattern in the precipitation front, visible in both the vertical profile and the axial cross section at Positions 2–3 in Experiment 3, where the injection rate was increased after 2 PVs of the $BaCl_2$ solution were injected. This layering feature becomes apparent only beyond a certain distance from the side injection borehole, approximately 30 mm.

Compared to Experiments 1 and 2, Experiment 3 exhibits a noticeable deviation of the precipitation front toward the outlet (Figure 4c). Evidence suggests that this deviation was caused by improper penetration of epoxy resin into the outlet endcap, which was discovered upon disassembly of the core holder of Experiment 3. As described in the Methods section, the core samples were encased in epoxy resin prior to placement in the core holder. As a result, a small amount of resin infiltrated the outlet endcap during preparation, partially obstructing the rock cross section and diverting the fluid flow. While this flow deviation influenced barite deposition in the final centimeter of the core, there is no evidence that it affected the precipitation dynamics throughout the rest of the sample.

In addition to the global barite precipitation pattern visualized by XRCT scanning, the micro-structures of precipitated barite in the pore space were captured with BSE scanning at a much higher resolution, as shown in Figure 5. These BSE images were taken around the precipitation boundary at different locations across one thin section (Figure S3 in Supporting Information S1).

Two primary forms of barite accumulations are evident: needle-shaped, elongated particles sparsely distributed and growing from the grain surface (Figures 5b and 5d), and more dense, amorphous barite deposits in the pore bodies, loosely attached to the grain surface (Figures 5c, 5e, and 5f).

In addition, small inclusions of barite, not detected with XRCT, were also found within the established boundary, as highlighted in Figures 5g and 5h. Notably, these barite inclusions in the initial mixing zone are visible at a very high magnification and are located in the narrow pore throats.

It should be noted that the thin section preparation, as described in the Methods section, involves multiple potentially destructive steps. For example, drilling of a thin section requires fluid circulation, and sample

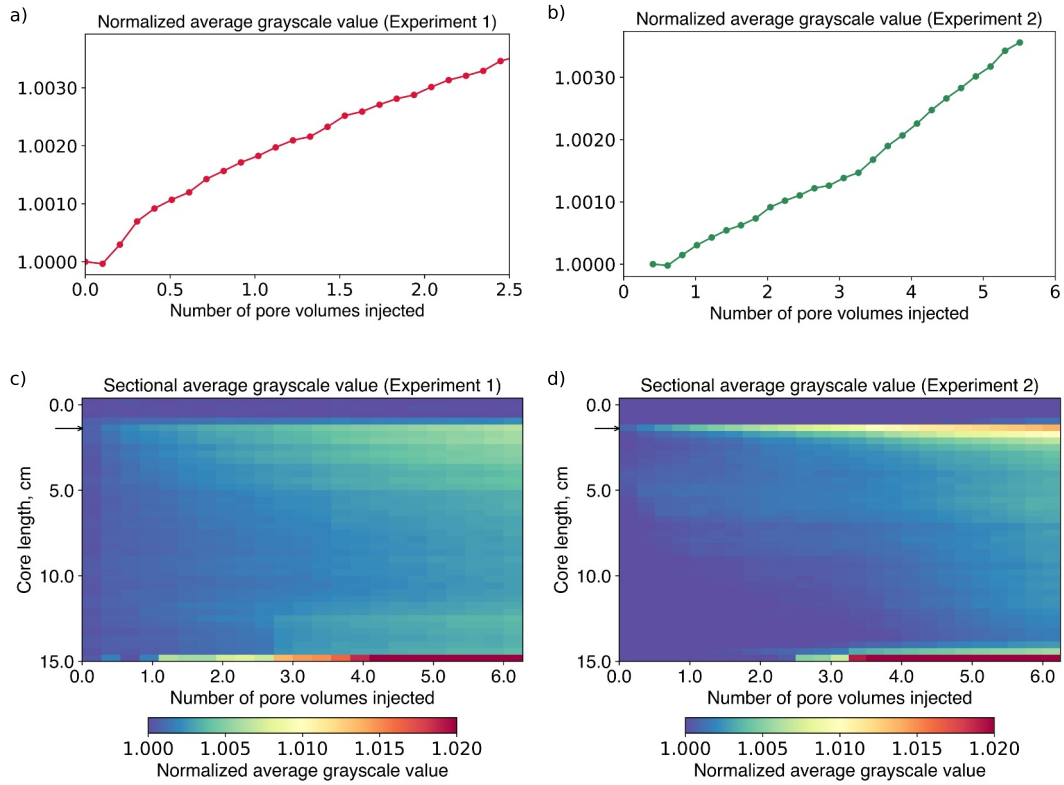

Figure 6. Temporal evolution of the normalized grayscale value for Experiments 1 and 2, calculated from the in situ 2D radiographs. Panels (a, b) show the temporal evolution of the normalized average grayscale values for the entire core sample, while Panels (c, d) present the spatial-temporal evolution of the normalized average grayscale values across multiple sections along the core length. All values were normalized against a baseline radiograph taken prior to the experiments. Values greater than 1 indicate an increase in mineral density compared to the baseline image, serving as a proxy for the increased barite content in the rock core.

impregnation with epoxy under vacuum might mobilize the unconsolidated particles in the pore space. With this in mind, we expect that the minerals detected with the measurement are in their true location and have not been displaced; however, deposits in the larger pores, which had less adhesion to the in situ grain surface, could have been removed. While this does not compromise the conclusions drawn from the analysis, it impedes precise element mapping across the entire cross section area.

3.2.1. Progression of Barite Precipitation

The in situ XRCT scanning technique allowed us to monitor the material density increase over time. By subtracting the baseline radiograph, we produced images that clearly illustrate the accumulation of barite deposits in the pore space. The images were rendered into animation sequences, namely Videos S1 and S2 for the respective experiments.

Using these radiographs, we conducted a quantitative analysis of barite precipitation propagation through the core length and its accumulation over time. Figure 6 presents the spatial-temporal evolution of barite precipitation based on the normalized average grayscale values obtained from the 2D radiographs. This analysis involved averaging the grayscale values for the entire core and for specific sections along its length and then normalizing these values against those from the baseline image. In our radiographs, the grayscale value increases with the mineral density, reflecting the extent of barite precipitation.

Initially subtle, the changes in average mineral density become increasingly visible over time, reflecting the ongoing barite deposition. Videos S1 and S2 show the rapid establishment of a thin initial boundary, followed by a steady increase in average mineral density and lateral growth toward the periphery of the core. Notably, a distinguishable boundary is established throughout the entire length of the core more quickly in the low flow rate

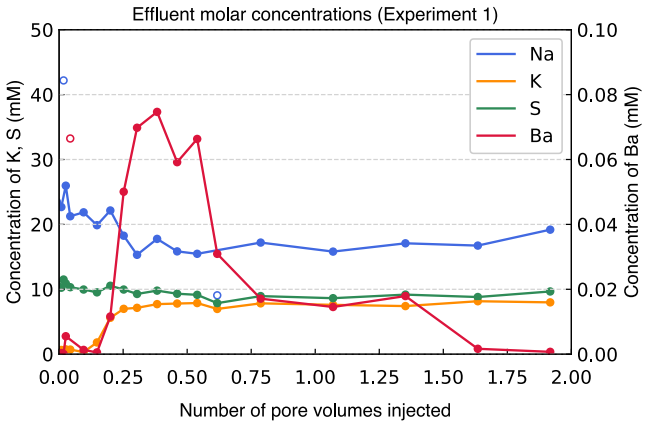

Figure 7. Temporal variation of cation molar concentrations in collected effluent as determined by inductively coupled plasma mass spectrometry. Empty data points represent outliers, based on the chemically reasonable Na/S ratio of the Na_2SO_4 solution.

scenario, occurring after approximately 1 PV injected, compared to around 3 PVs injected in the high flow rate case.

The analysis of the overall normalized grayscale values for the entire core (Figures 6a and 6b) shows a continuous increase, indicating a rise in average mineral density and hence, ongoing barite deposition in the rock core. This suggests that barite precipitation at the boundary continued steadily throughout the experiments, even if not always evident from the pressure measurements. The sectional spatial-temporal analysis indicates almost immediate barite precipitation near the side injection (highlighted by an arrow in Figures 6c and 6d). The precipitation continues to intensify over time, as evidenced by the step-wise increase in normalized grayscale values along the time axis in PVs.

A significant increase in normalized grayscale values was detected in the outlet section at ca. 1.5 and 3.0 PVs injected in Experiments 1 and 2, respectively, causing the overall pressure increase (Figure 2). Additionally, non-uniform precipitation near the outlet section of the core was observed in both experiments, with a more pronounced effect in Experiment 1. As shown in Figures 6c and 6d, the last 3 cm of the core exhibited more barite precipitation compared to the upper sections. This is attributed to the outlet blockage, which altered fluid flow paths, leading to enhanced reactant mixing and subsequent barite precipitation.

3.3. Evolution of Ion Concentrations in the Effluent

We analyzed the chemical composition of the effluents from Experiment 1 to track the progress of the chemical reaction. Figure 7 shows the concentration of Na, Ba, S, and K in the effluents against the cumulative injected volume (in PVs) of the $BaCl_2$ solution.

Molar concentrations of the analyzed elements reveal distinct behaviors of the reactant mixing and transport. Since potassium did not participate in the barite precipitation reaction and served as an inert tracer, its breakthrough curve can be assessed to estimate the volume occupied by the side injection solution and fluid mixing between the side and main injection. We observed that potassium breakthrough occurred at 0.2 PV injected, assessed at 50% of its stabilizing value. This timing coincides with the decrease of Na and S concentrations, reaching levels corresponding to the dilution ratio (6.7:1 from Table 1), indicating the mixing of two solutions and their subsequent transport.

High-level fluctuations of Na concentrations were observed within the first 0.3 PV of $BaCl_2$ solution injected. We attribute this variation to a small sampling volume (1–3 ml) in the early stage and the addition of 1 ml of 50 mM EDTA solution (containing Na), as described in the Methods Section. Thus, small uncertainties in the sample volume can be further magnified in the Na concentration determination. Nonetheless, the average Na concentration for this period is equal to 21.3 mM, which matches reasonably well with the initial concentration of the background solution.

We evaluated the barite precipitation reaction using the breakthrough curves of the reactants Ba^{2+} and SO_4^{2-}, with the latter inferred from the sulfur (^{32}S) content. As shown in the injection flow rate ratio (Table 1), Ba^{2+} is the limiting reactant, while SO_4^{2-} remains in significant excess, as clearly reflected in their breakthrough curves (Figure 7). The breakthrough of Ba^{2+} is delayed compared to potassium, occurring after 0.3 PV injected. Even post-breakthrough, Ba^{2+} concentrations remain up to two orders of magnitude below the theoretical maximum of 1.3 mM (assuming pure mixing). This indicates substantial consumption of Ba^{2+} due to the precipitation reaction.

Unlike the step-function-like breakthrough curve of potassium, which is typical for continuous injection, the Ba^{2+} breakthrough curve exhibits characteristics of a pulse injection, reflecting its varying consumption throughout different stages of the experiment. Notably, the peak at approximately 0.4 PV, the first significant drop at around 0.5, and the final decline at 0.8 PV align closely with the step-wise increase in average mineral density near the outlet, as shown in Figure 6c. These time points are attributed to the intensifying precipitation process in the outlet

endcap, where enhanced mixing leads to the increased consumption of Ba^{2+}. Moreover, the fluctuations in barium concentration between 1.3 and 2.0 PVs correspond to the previously discussed pressure oscillations.

4. Discussion

Our results reveal three key findings that elucidate the mechanisms of mineral precipitation in porous media: the evolution and propagation of the precipitation front, the effect of injection rate on the precipitation kinetics, and the subsequent reduction in permeability.

4.1. Mineral Precipitation: Front Development and Characterization

Understanding the mineral precipitation front development and its detailed characterization is important for designing effective remediation strategies for injectivity decline. Key parameters to examine include the shape, temporal evolution, location, and structure of the precipitated minerals and the front they form. Our post-experiment XRCT analyses depict a distinct precipitation front in the shape of a "curtain." A similar precipitation front has previously been observed in experiments in the context of groundwater-seawater mixing, leading to the deposition of iron (Fe) oxides (Cao et al., 2024; Zhao et al., 2023). In those column experiments, Fe(II) from groundwater oxidized upon contact with dissolved oxygen in seawater, forming a barrier in a porous medium. While the spatial and temporal scales of our work are different, the general curtain shape, governed by the advection and dispersion processes, resembles our experimental observations, suggesting a common underlying mechanism, driven by mixing-induced precipitation.

We attribute the curtain-like mineral precipitation front to the boundary between distinct flow paths in the core sample, resulting from the interaction of the axial (main) and side fluid injections. The side injection fluid is expected to primarily occupy the region inside the curtain, with precipitation reactions occurring mainly at the interface between the two fluids (i.e., solutions). Under steady-state flow conditions, the flow paths from the side injection align parallel to those of the main injection, as indicated by the precipitation front in Figure 4. This parallel flow assumption suggests equal specific discharge rates for side injection and main injection: $Q_{side}/A_{side} = Q_{main}/A_{main}$, leading to $(A_{core} - A_{side})/A_{side} = Q_{main}/Q_{side}$, where A represents the cross-sectional area. For the low flow rate scenario, with $Q_{main}/Q_{side} = 6.7$, $L_{side} = 13$ cm, and $L_{core} = 15$ cm, the estimated volume occupied by the side injection is $V_{side}/V_{core} = 15.0\%$ of the core volume, where $V = AL$. For the high flow rate scenario with $Q_{main}/Q_{side} = 5.7$, the estimated volume occupied by the side injection increases to $V_{side}/V_{core} = 17.2\%$ of the core volume. These estimates are consistent with the approximate volume ratio derived from the precipitation front observed in the XRCT images, as well as the breakthrough curves in Figure 7, which suggest a volume ratio of ~20%.

The thickening of the mineral precipitation front is attributed to the accumulation of barite, which depends on the competition between the transport of reactants and the chemical reaction. This competition is typically described by the Damköhler number. Previous numerical studies have shown that in reaction-dominated regimes, the dissolution/precipitation front tends to be sharp and narrow, while in the transport-dominated regimes, the reacting ions can propagate further before immediately clogging the porous medium, resulting in a thicker mineral front or curtain (Koehn et al., 2021; Szymczak & Ladd, 2009; Tartakovsky et al., 2008). Based on the calculated Damköhler and Péclet numbers (Text S1, Equations S3–S6 in Supporting Information S1), our experimental observations align well with the described mechanisms. We observe clear, well-defined precipitation boundaries under low Péclet numbers (2.19 and 3.72 for low- and high-flow rate cases, respectively) and a thicker precipitation front in the case of lower Damköhler number (0.64×10^{-5} under high flow rate conditions against 1.08×10^{-5} under low flow rate conditions).

The in situ XRCT images (Figure 6) and pressure response (Figure 2) reveal the progression of the precipitation front over time. Before the complete injection of one pore volume (PV) of the side injection solution, a distinct mineral precipitation front, visible in the XRCT images, has already been established. This front becomes more pronounced as the precipitated barite accumulates along the pre-defined boundary. Our XRCT observations align well with the differential pressure measurements, which show a continuous decline in permeability, consistent with ongoing barite precipitation. The gradual thickening of the precipitation front leads to an increased impact on permeability. This suggests that the precipitation front was initially established due to the strong mixing during the initial fluid displacement (the reaction-dominated regime), with subsequent precipitation (front thickening)

being transport-controlled. A previous study by Bray et al. (2016) suggested that as permeability in the precipitation zone decreases, molecular diffusion becomes the dominant transport mechanism. Our observations corroborate this suggestion, as the growth of the precipitation front slows significantly during the later stages of the experiments. This finding is also consistent with the numerical work of Ahkami et al. (2020), which showed that the precipitation reaction and the associated permeability decline progress more slowly in the diffusive regime.

A few barite inclusions were identified within the side injection region inside the precipitation curtain (Figures 5g and 5h). These inclusions suggest that the initial fluid mixing during fluid displacement led to minor barite deposits, particularly in regions of low flow velocity. However, these early deposits did not cause an immediate reduction in permeability.

High-resolution BSE images of barite deposits reveal substantial pore blockage and reduced pore connectivity (Figure 5). However, the deposited barite also exhibits porous structures, leaving some pore space unfilled, which leads to secondary porosity in the original pore space. Previous experimental and numerical studies suggest that mineral deposits can substantially alter the pore connectivity while retaining micro-porosity (Chagneau et al., 2015; Deng et al., 2021; Poonoosamy et al., 2020). Our observations confirm this phenomenon, showing that the retained micro-porosity plays a key role in promoting the diffusion-controlled thickening of the mineral precipitation front, observed during the later stages of the core-flooding experiments. By limiting advective transport across the precipitation boundary, this micro-porosity promotes further reactions as well as lateral growth of the precipitation front.

4.2. Effect of Flow Velocities on Fluid Mixing and Precipitation Kinetics

Reactant mixing is a crucial factor in mineral precipitation front development, and it is strongly influenced by flow velocities, as evidenced when comparing high-resolution XRCT images from Experiments 1 and 2 (Figure 4). Higher pore velocities increase lateral mechanical dispersion, enhancing the mixing of reacting ions in the pore space and thickening the precipitation front. We acknowledge that different pore volumes (PVs) were injected in Experiments 1 and 2, and that longer exposure time may contribute to increased mineral accumulation. However, comparisons of 2D radiographs (Videos S1 and S2) at equivalent injection stages, matched by PVs injected, show observable differences in front thickness attributable to flow velocity, supporting our conclusion that higher flow rates promote the development of thicker precipitation fronts.

Our observations align well with several numerical and experimental studies (Tartakovsky et al., 2008; Yang et al., 2024). For instance, a recent microfluidics study by Yang et al. (2024) demonstrated how fluid inertia controls mineral precipitation and fluid flow path clogging at flow intersections. Their work reveals distinct precipitation regimes as a function of Reynolds number, where lower Reynolds numbers lead to thin, dense layers of precipitation that effectively shut off further mineral precipitation, while higher Reynolds numbers facilitate rapid flow path clogging due to enhanced precipitation across the entire flow intersection. Yang et al. (2024) additionally highlight the precipitation enhancement effect when fluids with different flow rates are mixed. Our observations extend these findings to precipitation reactions in porous media, showing similar effects across a range of flow velocities, as reported in Tables 1 and S1 in Supporting Information S1.

Differences in fluid injection rate ratios introduce further variations in the thickness of the developing mineral precipitation front along the main flow direction. With the fluid side injection introduced perpendicular to the main flow, strong mixing occurred near the side injection borehole due to the lateral component of the side injection. As the side flow is redirected by the "background" (core-axial) flow toward the outlet, mixing becomes less pronounced as the flow paths of both injections align in the downstream direction, resulting in a thinner mineral precipitation front. The correlation between the ratio of co-injected fluid flow rates (consequently, their mixing) and the thickness of the resulting front has previously been reported by Bray et al. (2016). While we do not directly compare front thickness values due to differences in experiment setups, chemicals, and porous media, our findings support this relationship and extend it to a different injection scheme.

The described effect is also evident in the calculated formation damage coefficients, which are consistently higher in the top section than in the middle section (Figure 3). This difference reflects the stronger mixing near the injection borehole, where the lateral flow component enhances reactant interaction and thus promotes more extensive precipitation. In contrast, the formation damage induced by the further parallel flow of reactive species

within the middle section is less pronounced. Previously reported values of formation damage coefficient for mineral precipitation based on laboratory data cover a wide range, from 10 to 3,000 (Bedrikovetsky et al., 2009; Carageorgos et al., 2010). Vaz et al. (2016) reported lower values (0.1–0.7), corresponding to lining-type deposition creating minimal hydraulic resistance to the flow. The values calculated in our experiments fall within the reported range.

A comparison of in situ radiographs (Figure 6) between Experiments 1 and 2 reveals a clear difference in the timing of front establishment. Specifically, in the high flow rate scenario, establishment of a distinguishable boundary throughout the whole length of the core is delayed, compared to the low flow rate case. This observation supports the hypothesis that higher flow rates enhance fluid mixing, leading to greater consumption of the reactants upstream, thereby significantly reducing the chemical affinity for precipitation reactions downstream. Nonetheless, during advection-dominated transport, reactants can propagate deeper into the porous medium, compared to diffusion-controlled scenarios, as demonstrated in previous numerical studies (Koehn et al., 2021; Li et al., 2008). Our results show that increasing the flow rate, and consequently the Péclet number, from 2.19 to 3.72, results in a thicker mineral precipitation front. The enhanced mixing accelerates the overall reactions, leading to higher consumption rates of the reacting ions, increased barite deposition in the pore space, and a thickening of the precipitation front.

Our post-experiment BSE characterization (Figure 5) shows a clear correlation between precipitation behavior and transport regimes in the precipitation region. Previous studies have shown that mineral precipitations in high-velocity regions are transport-controlled, occurring predominantly near pore throats, whereas surface reaction-controlled processes are accompanied by mineral growth around grain surfaces (Wetzel et al., 2020). The morphology and distribution of the precipitated minerals allow us to infer the precipitation dynamics across the zones with different pore velocities. Needle-like deposits (Figure 5d) suggest less interrupted mineral growth in regions with lower interstitial velocities, indicative of diffusion-controlled mixing, leading to regions that are not fully obstructed by mineral deposits. Conversely, zones with larger, less structured mineral deposits (Figure 5b) and substantial porosity reductions, correspond to high-velocity regions, characterized by pronounced mixing and fluid-fluid interactions. Despite reductions in porosity, residual micro-porosity still enables fluid penetration at relatively high velocities, as evidenced by the double front formation in the mixed flow rate experiment, where the side fluid injection rate was increased during the later stage of the experiment (Figure 4c). This observation aligns with field examples of fluid injectivity decline, where injectivity dropped drastically but never reached zero (Brehme et al., 2018, 2024), indicating that residual secondary porosity persists, maintaining permeability for continued fluid flow.

4.3. Permeability Reduction Due To Mineral Precipitation

Our results suggest a significant reduction in bulk permeability by 10%–20%, due to barite precipitation, even though the precipitation front aligns with the axial flow. The initial immediate permeability drop of approximately 10% is attributed to the introduction of side fluid flow, which re-establishes steady-state flow conditions. Under steady-state flow conditions alone, bulk permeability would be expected to recover. However, no recovery was recorded, as the permeability reduction intensified due to barite precipitation at the fluids' interface, governed by the flow rate ratios as shown in Figure 4 within the first minutes of co-injection. The high kinetic rate, combined with the low solubility of barite in aqueous solutions, resulted in the “shelter hut” formation, that is, blockage of the regions above the side injection borehole. XRCT images estimate that the cross-sectional area of this shelter hut, and eventually the overall mineral precipitation curtain, constitutes 15%–17% of the total rock cross-sectional area. This zone separation by the precipitation front leads to the described permeability drop.

As the front thickened and barite deposition intensified, evidenced by increased differential pressure, further reduction in bulk permeability occurred in smaller increments. The continued precipitation is estimated to cause an additional 10% reduction in bulk permeability. While previous experimental flow-through studies have reported greater reductions in permeability, up to 50 and even 95% reduction from initial values (Noiriel et al., 2016; Orywall et al., 2017), these variations are highly influenced by the experiment design and the distribution of incompatible fluids in the pore space. Our study illustrates that flow distribution patterns significantly influence rock permeability.

However, different timescales of the process should be acknowledged, as the mentioned reduction in permeability was achieved ca. two times faster in the low flow rate case. This is additionally highlighted by the formation damage coefficient values. Even though injection at a higher flow rate, as shown by the in situ XRCT scanning, results in a larger mixing front and, consequently, thicker mineral precipitation boundary, the impact of this boundary on the overall rock permeability is slower. As seen by the post-experiment BSE images, not all the pores are occupied with barite completely and still have remaining micro-porosity. We believe that in the low flow rate scenario the effect of longer residence time plays a role in promoting the chemical reaction at the fluids contact, hence creating a thinner but less permeable boundary.

Furthermore, the permeability of the precipitation front is an important aspect to address. Post-experiment XRCT images (Figure 6c) depict a distinctive double-front structure in Experiment 3: a thin inner front, similar to the low flow rate scenario in Experiment 1, and a wider outer front, resembling the high flow rate scenario of Experiment 2. Notably, this double-front pattern becomes evident only at a certain distance from the side injection borehole (approximately 30 mm). This phenomenon could be attributed to substantial barite precipitation occurring in the top section of the specimen, where enhanced mixing, caused by the lateral component of the side injection, results in more effective clogging of a large number of pores. This clogging, in turn, substantially decreases porosity and permeability near the side injection, creating a tight "skin" that limits the expansion of the side flow, even with an increased injection rate. As a result, it is only beyond a certain distance from the injection point, where the inner front becomes permeable enough so that the side flow can penetrate the inner front, which is likely caused by dislodging loosely connected particles, which then move downstream. This penetration promotes further reactant mixing outside the initially established inner front, leading to the observed double front structure. We also see how the formation damage coefficient in the middle zone began to dominate after the switch in flow rates—an effect not observed in any other scenario. This distinction is further supported by XRCT imaging, which shows that reactive ions propagated into the lower parts of the core, enhancing formation damage and impacting the permeability of the already-established boundary. This process would also explain the slight improvement in permeability, observed during the switch of the flow rates in Experiment 3.

The formation damage coefficient facilitates the assessing of a system's susceptibility to clogging and can serve as a bridge between laboratory observations and field-scale predictions. Although the injection strategy employed in our experiments is tailored to a specific setup, the calculated values may further be used to estimate the impact of mineral precipitation on system's performance under field conditions, using established calculation methods (Bedrikovetsky et al., 2009). With appropriate boundary conditions and scaling considerations, these lab-derived coefficients offer valuable insights into the extent and evolution of formation damage in operational geothermal or subsurface injection systems.

It is also important to acknowledge the pronounced fluid blockage observed at the outlet endcap and its impact on the pressure response. Barite precipitation is expected to accelerate when reactants reach the endcap in sufficient concentrations, as the confined space and associated flow line convergence enhance reactant mixing, leading to rapid mineral precipitation, outlet blockage, and sharp pressure increases. This was confirmed with pressure measurements (Figure 2) and XRCT imaging (Figures 4 and 6). This localized blockage at the outlet is evidenced by the consistent rising of pressures from both main and side fluid injections and by the absence of a significant increase in the differential fluid pressures across the top and the middle sections of the rock core. These observations highlight the relationship between localized permeability and precipitation intensity, showing that the introduction of incompatible fluids into high-permeability zones strongly enhances reactant mixing, accelerating mineral precipitation reactions. This agrees with earlier research (Ahkami et al., 2020), which highlighted the strong influence of flow into high-permeable zones on mineral precipitation patterns in fractured porous media. The observed behavior suggests that such effects could be particularly severe in heterogeneous reservoirs with dual-porosities, where permeable zones could accelerate chemical reactions, underscoring the importance of further research into effective control strategies for sustaining injectivity.

5. Conclusions

This study advances the current understanding of mineral precipitation in porous media during co-injection of two incompatible fluids, offering key insights into the distribution of the precipitation front, the effects of flow rate on precipitation kinetics, and the consequent reductions in bulk permeability. Through core-flooding experiments,

accompanied by various high-resolution imaging techniques, we characterize the dynamic evolution of precipitation fronts, focusing on their location, growth patterns, and impact on pore connectivity.

We establish a distinct "curtain"-like shape of the formed mineral precipitation front, which is governed by the flow patterns arising from the interaction between axial (main) and side fluid injections. The side injection fluid primarily occupied the region within the curtain, while mineral precipitations occurred mainly at the fluid interface. The fluid flow rate was found to be a critical factor influencing mineral precipitation kinetics, as higher flow rates intensify fluid (i.e., reactant) mixing, causing thicker mineral precipitation fronts and more substantial mineral accumulations in the pore space.

Additionally, we explore how continuous mineral precipitation shifts the balance between advection and diffusion processes within the precipitation zone. Initially, the precipitation front was formed under a reaction-dominated regime, followed by transport-controlled front thickening as mineral precipitation progressed.

Despite the reduction in porosity due to barite precipitation, residual micro-porosity facilitates continued solute transport, contributing to further growth and lateral expansion of the mineral precipitation front. This is evidenced by the formation of a double-front structure in the mixed flow rate scenario, where increased side injection flow rates enabled the penetration of fluids and reactants into the inner front, dislodging loosely connected particles and promoting further mixing, transport, and mineral precipitation reactions.

In situ XRCT imaging, in combination with differential pressure measurements, proved to be an effective technique for capturing real-time precipitation processes. While XRCT imaging is subject to resolution limitations, it provides valuable insights into the spatial distribution of precipitates and the development of the mineral precipitation front. Post-experiment 3D scanning and BSE imaging offered additional information on mineral morphology and pore space evolution, reinforcing the benefit of multi-technique approaches when studying complex mineral precipitation dynamics.

While our experiments provide critical insights into mineral precipitation processes, they were conducted under controlled laboratory conditions. Natural porous media often exhibit greater heterogeneity, leading to more varied flow path geometries and complex mineral precipitation patterns. Further studies are required to investigate the impact of different porous media heterogeneities and the influence of diverse mineral compositions in natural settings. Moreover, the long-term stability of precipitated minerals under continuous fluid injection conditions is another critical aspect that should be investigated. Understanding the extent to which precipitated particles can be dislodged and transported and how this affects downstream permeabilities is essential to predict the long-term evolution of fluid paths in order to prevent decreases in reservoir performance.

Nomenclature

A	Cross-sectional area [L^2]
$C_{Ba^{2+}}$	Concentration of Ba^{2+} in the injected solution [$N\ L^{-3}$]
$C^{eq}_{Ba^{2+}}$	Equilibrium concentration of Ba^{2+} [$N\ L^{-3}$]
ΔP	Pressure drop [$M\ L^{-1}\ T^{-2}$]
d_b	Injection "borehole" diameter [L]
d_c	Core sample diameter [L]
d_p	Dominant pore size [L]
D	Diffusivity [$L^2\ T^{-1}$]
J	Impedance index [–]
h	Reservoir thickness [L]
k	Permeability [L^2]
k_r	Reaction rate constant [$N\ L^{-2}\ T^{-1}$]
l_b	Injection "borehole" length [L]
L	Sample length [L]
m	Impedance growth coefficient [–]
M_{BaSO_4}	Molecular weight of barite [$M\ N^{-1}$]
q	Specific discharge [$L\ T^{-1}$]
Q	Volumetric injection rate [$L^3\ T^{-1}$]
r	Radial distance from the wellbore [L]

R	Reaction rate [L T^{-1}]
t	Time [T]
v	Interstitial velocity [L T^{-1}]
V_m	Molar volume [L^3 N^{-1}]
Pe	Péclet number [–]
Re	Reynolds number [–]
Da_I	Damköhler number I [–]
Da_{II}	Damköhler number II [–]

Greek Symbols

β	Formation damage coefficient [–]
μ	Dynamic viscosity [M L^{-1} T^{-1}]
ρ	Density [M L^{-3}]
ϕ	Porosity [–]

Abbreviations

BSE	Backscattered Electron Images
EDS	Energy Dispersive Spectrometry
EDTA	Ethylene Diamine Tetraacetic Acid
EPMA	Electron Probe Microanalyzer
ICP-MS	Inductively Coupled Plasma Mass Spectrometry
PV	Pore Volume
SEM	Scanning Electron Microscopy
WDS	Wavelength Dispersive Spectrometry
XRCT	X-ray Computed Tomography
XRD	X-ray Diffraction

Data Availability Statement

The data supporting the results in this manuscript are available in Kottsova (2024) [Data set].

Acknowledgments

The authors would like to thank Dr. Claudio Madonna for his assistance with core drilling, Ning Ma for his help with the X-ray diffraction measurements, and Andreas Jallaz for his support in thin section preparation. The authors also thank the Reviewers for the extensive review of the manuscript. The EASYGO project (easygo-itn.eu) has received funding from the European Union's Horizon 2020 Research and Innovation Programme under the Marie Skłodowska-Curie Grant 956965. The authors also highly appreciate the support by Energi Simulation. The Werner Siemens Foundation (Werner Siemens-Stiftung–WSS) is further thanked for its support of the Geothermal Energy and Geofluids (GEG) group (https://geg.ethz.ch) at ETH Zurich (ETHZ), Switzerland. Open access publishing facilitated by Eidgenossische Technische Hochschule Zurich, as part of the Wiley - Eidgenossische Technische Hochschule Zurich agreement via the Consortium Of Swiss Academic Libraries.

References

Ahkami, M., Parmigiani, A., Di Palma, P. R., Saar, M. O., & Kong, X.-Z. (2020). A lattice-Boltzmann study of permeability-porosity relationships and mineral precipitation patterns in fractured porous media. *Computational Geosciences*, *24*(5), 1865–1882. https://doi.org/10.1007/s10596-019-09926-4

Al-Kaabi, F. S., Hussein, R. A., & Abdulkareem, M. A. (2023). Dissolution of barite using coordination chemistry: Optimization and characterization. *Results in Chemistry*, *5*, 100791. https://doi.org/10.1016/j.rechem.2023.100791

Axelsson, G. (2012). Role and management of geothermal reinjection. In *Short course on geothermal development and geothermal wells* (pp. 1–21). UNU-GTP and LaGeo.

Bedrikovetsky, P., Mackay, E., Silva, R., Patricio, F., & Rosário, F. (2009). Produced water re-injection with seawater treated by sulphate reduction plant: Injectivity decline, analytical model. *Journal of Petroleum Science and Engineering*, *68*(1–2), 19–28. https://doi.org/10.1016/j.petrol.2009.05.015

Bedrikovetsky, P., Marchesin, D., Shecaira, F., Souza, A., Milanez, P., & Rezende, E. (2001). Characterisation of deep bed filtration system from laboratory pressure drop measurements. *Journal of Petroleum Science and Engineering*, *32*(2–4), 167–177. https://doi.org/10.1016/s0920-4105(01)00159-0

Bray, J. M., Lauchnor, E. G., Redden, G. D., Gerlach, R., Fujita, Y., Codd, S. L., & Seymour, J. D. (2016). Impact of mineral precipitation on flow and mixing in porous media determined by microcomputed tomography and MRI. *Environmental Science and Technology*, *51*(3), 1562–1569. https://doi.org/10.1021/acs.est.6b02999

Brehme, M., Markó, Á., Osvald, M., Zimmermann, G., Weinzierl, W., Aldaz, S., et al. (2024). Demonstration of a successful soft chemical stimulation in a geothermal sandstone reservoir in mezőberény (Hungary). *Geothermics*, *120*, 102980. https://doi.org/10.1016/j.geothermics.2024.102980

Brehme, M., Nowak, K., Banks, D., Petrauskas, S., Valickas, R., Bauer, K., et al. (2019). A review of the hydrochemistry of a deep sedimentary aquifer and its consequences for geothermal operation: Klaipeda, Lithuania. *Geofluids*, *2019*, 1–20. https://doi.org/10.1155/2019/4363592

Brehme, M., Regenspurg, S., Leary, P., Bulut, F., Milsch, H., Petrauskas, S., et al. (2018). Injection-triggered occlusion of flow pathways in geothermal operations. *Geofluids*, *2018*, 1–14. https://doi.org/10.1155/2018/4694829

Cao, W., Yan, G., Hofmann, H., & Scheuermann, A. (2024). State of the art on fe precipitation in porous media: Hydrogeochemical processes and evolving parameters. *Journal of Marine Science and Engineering*, *12*(4), 690. https://doi.org/10.3390/jmse12040690

Carageorgos, T., Marotti, M., & Bedrikovetsky, P. (2010). A new laboratory method for evaluation of sulfate scaling parameters from pressure measurements. *SPE Reservoir Evaluation and Engineering*, *13*(3), 438–448. https://doi.org/10.2118/112500-pa

Chagneau, A., Claret, F., Enzmann, F., Kersten, M., Heck, S., Madé, B., & Schäfer, T. (2015). Mineral precipitation-induced porosity reduction and its effect on transport parameters in diffusion-controlled porous media. *Geochemical Transactions*, *16*(1), 13. https://doi.org/10.1186/s12932-015-0027-z

Deng, H., Tournassat, C., Molins, S., Claret, F., & Steefel, C. I. (2021). A pore-scale investigation of mineral precipitation driven diffusivity change at the column-scale. *Water Resources Research*, *57*(5). https://doi.org/10.1029/2020wr028483

Haynes, W. (Ed.). (2014). *CRC handbook of chemistry and physics* (95th ed.). CRC Press.

Kastner, J., & Heinzl, C. (2020). X-ray tomography. In *Handbook of advanced nondestructive evaluation* (pp. 1–73). Springer International Publishing. https://doi.org/10.1007/978-3-319-30050-4_5-2

Kaya, E., Zarrouk, S. J., & O'Sullivan, M. J. (2011). Reinjection in geothermal fields: A review of worldwide experience. *Renewable and Sustainable Energy Reviews*, *15*(1), 47–68. https://doi.org/10.1016/j.rser.2010.07.032

Koehn, D., Piazolo, S., Beaudoin, N. E., Kelka, U., Spruženiece, L., Putnis, C. V., & Toussaint, R. (2021). Relative rates of fluid advection, elemental diffusion and replacement govern reaction front patterns. *Earth and Planetary Science Letters*, *565*, 116950. https://doi.org/10.1016/j.epsl.2021.116950

Kottsova, A. (2024). Pressure and ICP-MS data from core flooding experiments on mineral precipitation in porous media [Dataset]. *ETH Zurich Research Collection*. https://doi.org/10.3929/ethz-b-000702479

Kottsova, A., Bruhn, D., Saar, M. O., Veeger, F., & Brehme, M. (2022). *Clogging mechanisms in geothermal operations: Theoretical examples and an applied study* (pp. 1–6). European Geothermal Congress.

Li, X., Huang, H., & Meakin, P. (2008). Level set simulation of coupled advection-diffusion and pore structure evolution due to mineral precipitation in porous media. *Water Resources Research*, *44*(12). https://doi.org/10.1029/2007wr006742

Lima, M. G., Javanmard, H., Vogler, D., Saar, M. O., & Kong, X.-Z. (2021). Flow-through drying during CO_2 injection into brine-filled natural fractures: A tale of effective normal stress. *International Journal of Greenhouse Gas Control*, *109*, 103378. https://doi.org/10.1016/j.ijggc.2021.103378

Luo, W., Kottsova, A., Vardon, P., Dieudonné, A., & Brehme, M. (2023). Mechanisms causing injectivity decline and enhancement in geothermal projects. *Renewable and Sustainable Energy Reviews*, *185*, 15. https://doi.org/10.1016/j.rser.2023.113623

Majer, E. L., & Peterson, J. E. (2007). The impact of injection on seismicity at the geysers, California geothermal field. *International Journal of Rock Mechanics and Mining Sciences*, *44*(8), 1079–1090. https://doi.org/10.1016/j.ijrmms.2007.07.023

Mason, D. L., Clark, G. W., Barton, D., More, S., Scott, J., & Keating, D. (2023). *pydicom: An open source dicom library*. Zenodo. https://doi.org/10.5281/zenodo.10385252

Noiriel, C., Steefel, C. I., Yang, L., & Bernard, D. (2016). Effects of pore-scale precipitation on permeability and flow. *Advances in Water Resources*, *95*, 125–137. https://doi.org/10.1016/j.advwatres.2015.11.013

Orywall, P., Drüppel, K., Kuhn, D., Kohl, T., Zimmermann, M., & Eiche, E. (2017). Flow-through experiments on the interaction of sandstone with Ba-rich fluids at geothermal conditions. *Geothermal Energy*, *5*(1), 20. https://doi.org/10.1186/s40517-017-0079-7

Poonoosamy, J., Haber-Pohlmeier, S., Deng, H., Deissmann, G., Klinkenberg, M., Gizatullin, B., et al. (2020). Combination of MRI and SEM to assess changes in the chemical properties and permeability of porous media due to barite precipitation. *Minerals*, *10*(3), 226. https://doi.org/10.3390/min10030226

Raies, I., Kohler, E., Fleury, M., Pédel, N., & Ledésert, B. (2023). Formation damage induced by clay colloids deposition in Triassic clastic geothermal fields: Insights from an experimental approach. *Applied Clay Science*, *234*, 106868. https://doi.org/10.1016/j.clay.2023.106868

Rosenbauer, R. J., Bischoff, J. L., & Kharaka, Y. K. (1992). Geochemical effects of deep-well injection of the paradox valley brine into Paleozoic carbonate rocks, Colorado, U.S.A. *Applied Geochemistry*, *7*(3), 273–286. https://doi.org/10.1016/0883-2927(92)90043-3

Shafabakhsh, P., Cordonnier, B., Pluymakers, A., Le Borgne, T., Mathiesen, J., Linga, G., et al. (2024). 4D neutron imaging of solute transport and fluid flow in sandstone before and after mineral precipitation. *Water Resources Research*, *60*(3). https://doi.org/10.1029/2023wr036293

Stark, M. A., Box, W. T., Beall, J. J., Goyal, K. P., & Pingol, A. S. (2005). The Santa Rosa – Geysers recharge project, geysers geothermal field, California, USA. In *Proceedings World Geothermal Congress 2005* (pp. 24–29).

Szanyi, J., Medgyes, T., Kóbor, B., & Tari, C. (2014). *Experiences with geothermal water injection into porous aquifers* (Vol. 53). Technika Poszukiwa'balamurugan n Geologicznych.

Szymczak, P., & Ladd, A. J. C. (2009). Wormhole formation in dissolving fractures. *Journal of Geophysical Research: Solid Earth*, *114*(B6). https://doi.org/10.1029/2008jb006122

Tartakovsky, A. M., Redden, G., Lichtner, P. C., Scheibe, T. D., & Meakin, P. (2008). Mixing-induced precipitation: Experimental study and multiscale numerical analysis. *Water Resources Research*, *44*(6). https://doi.org/10.1029/2006wr005725

Vance, D., Matthews, A., Keech, A., Archer, C., Hudson, G., Pett-Ridge, J., & Chadwick, O. A. (2016). The behaviour of Cu and Zn isotopes during soil development: Controls on the dissolved load of rivers. *Chemical Geology*, *445*, 36–53. https://doi.org/10.1016/j.chemgeo.2016.06.002

Vaz, A., Maffra, D., Carageorgos, T., & Bedrikovetsky, P. (2016). Characterisation of formation damage during reactive flows in porous media. *Journal of Natural Gas Science and Engineering*, *34*, 1422–1433. https://doi.org/10.1016/j.jngse.2016.08.016

Virtanen, P., Gommers, R., Oliphant, T. E., Haberland, M., Reddy, T., Cournapeau, D., & SciPy 1.0 Contributors. (2020). SciPy 1.0: Fundamental algorithms for scientific computing in python. *Nature Methods*, *17*(3), 261–272. https://doi.org/10.1038/s41592-019-0686-2

Wetzel, M., Kempka, T., & Kühn, M. (2020). Hydraulic and mechanical impacts of pore space alterations within a sandstone quantified by a flow velocity-dependent precipitation approach. *Materials*, *13*(14), 3100. https://doi.org/10.3390/ma13143100

Yang, W., Chen, M. A., Lee, S. H., & Kang, P. K. (2024). Fluid inertia controls mineral precipitation and clogging in pore to network-scale flows. *Proceedings of the National Academy of Sciences*, *121*(28), e2401318121. https://doi.org/10.1073/pnas.2401318121

Yildirim, N., & Simsek, S. (2003). Determination of appropriate injection conditions for Kizildere geothermal waste fluid to avoid scale formation and cooling. In *European geothermal conference* (pp. 1–8).

Zhao, Z., Zhang, C., Cao, W., Hofmann, H., Wang, T., & Li, L. (2023). Oxidative precipitation of Fe(II) in porous media: Laboratory experiment and numerical simulation. *ACS ES and T Water*, *3*(4), 963–973. https://doi.org/10.1021/acsestwater.2c00458

Zhen-Wu, B., Dideriksen, K., Olsson, J., Raahauge, P., Stipp, S., & Oelkers, E. (2016). Experimental determination of barite dissolution and precipitation rates as a function of temperature and aqueous fluid composition. *Geochimica et Cosmochimica Acta*, *194*, 193–210. https://doi.org/10.1016/j.gca.2016.08.041

References From the Supporting Information

Palandri, J. L., & Kharaka, Y. K. (2004). A compilation of rate parameters of watermineral interaction kinetics for application to geochemical modeling [Open File Report]. (2004-1068). (Prepared in cooperation with the National Energy Technology Laboratory – United States Department of Energy).